EUMETSAT Contract No. EUM/CO/18/4600002180/JML

EVOLUTIONS STUDIES AUTOMATED OPTICAL SENSOR REGISTRATION MONITORING TOOL

State of the Art

Deliverable D04

Prepared by

Ursula FASCHING, Stefan SCHEIBLAUER and Thomas NAGLER
ENVEO IT, Innsbruck, AUSTRIA

Document Reference: ENVEO-OSMON_SOA_D04
Issue / Revision: 1/2
Date: 18.07.2019

Document controlled by Stefan Scheiblauer

This page is intentionally left blank.

EUMETSAT STUDY CONTRACT REPORT

CONTRACT NO:	**SUBJECT:**		**CONTRACTOR:**
EUM/CO/18/4600002180/JML	State of the Art		ENVEO
	STAR CODE:	NO OF VOLUMES: 1 THIS IS VOLUME NO: 1	CONTRACTOR'S REF: Deliverable D04

ABSTRACT:

This document reviews open literature regarding the validation of the geolocation of optical satellite data according to generic requirement [R-2]. The review includes applicable methods and systems for accuracy assessment of medium resolution sensors and high-resolution sensors. Published tools for geo-location assessment of MROI data will be reviewed and assessed, including procedures developed in the ESA project GEOACCA (PI: T. Nagler ENVEO; Nagler et al, 2016). Suitable algorithms are identified, and tests with various types of reference data and satellite data are performed with focus on AVHRR, SLSTR, and OLCI.

The evaluation gives an overview on the state of the art of methods and available software tools and libraries (Req. 1.). This document summarizes the outcome of WP-2.1.

AUTHORS:
STEFAN SCHEIBLAUER, THOMAS NAGLER, URSULA FASCHING,

EUMETSAT STUDY MANAGER:	EUMETSAT BUDGET HEADING
Johannes Müller	

This page is intentionally left blank.

DOCUMENT CHANGE LOG

Issue/ Revision	Date	Modification	Modified pages	Observations
1.0	12/11/2018	All new	All	-
1.1	21/2/2019	Comments by EUMETSAT	-	Added comments by EUMETSAT
1.2	18/7/2019	Added © EUMETSAT	All	Added © EUMETSAT in footers of all pages

This page is intentionally left blank.

TABLE OF CONTENT

ACCRONYMS

AATSR	Advanced Along-Track Scanning Radiometer
ATSR-2	Along-Track Scanning Radiometer - 2
AVHRR	Advanced Very-High-Resolution Radiometer
BEAM	Basic ERS & Envisat (A)ATSR and Meris Toolbox
CAPS	Canadian AVHRR Processing System
DEM	digital elevation model
ESA	European Space Agency
ETM+	Enhanced Thematic Mapper Plus (sensor on-board LANDSAT 7)
FRS	full resolution full swath
FOV	field of view
GCP	Ground Control Point
GeoAcca	Feasibility Study for Geolocation Assessment of Optical Sensors
geocal site	ground control point collection (geometric calibration site)
GSD	Ground Sample Distance
LSF	line spread function
NDVI	Normalized Difference Vegetation index
MERIS	Medium Resolution Imaging Spectrometer
MODIS	Moderate Resolution Imaging Spectroradiometer
NIR	near infrared
NOAA	National Oceanic and Atmospheric Administration
OpenCV	Open Source Computer Vision Library
PAN	panchromatic
PROBA-V	Project for On-Board Autonomy - Vegetation
PSF	point-spread function
QB02	QuickBird-2

RMSE	root mean square error
SANA	Subpixel Automatic Navigation of AVHRR
SNPP	Suomi National Polar-orbiting Partnership
TIR	thermal infrared
TM	Thematic Mapper (sensor on-board LANDSAT 4 and LANDSAT 5)
VHR	very high resolution
VIIRS	Visible Infrared Imaging Radiometer Suite
WV01	WorldView-1

1. INTRODUCTION

1.1 *Purpose*

This document reviews open literature regarding the validation of the geolocation of optical satellite data according to generic requirement [R-2]. The review includes applicable methods and systems for accuracy assessment of medium resolution sensors and high-resolution sensors. Published tools for geo-location assessment of MROI data will be reviewed and assessed, including procedures developed in the ESA project GEOACCA (PI: T. Nagler ENVEO; Nagler et al, 2016). Suitable algorithms are identified, and tests with various types of reference data and satellite data are performed with focus on AVHRR, SLSTR, and OLCI.

The evaluation gives an overview on the state of the art of methods and available software tools and libraries (Req. 1.). This document summarizes the outcome of WP-2.1.

1.2 *Outline*

In Section 2, the requirements for geolocation are described. In section 3, open literature related to the assessment of the geolocation accuracy of optical satellite data is reviewed.

2. REQUIREMENTS FOR GEOLOCATION

Precise geolocation of satellite imagery is fundamental for systematic climate observations. It allows to monitor the Essential Climate Variables (ECVs) stated by the Global Climate Observing System. Consequently, multi-sensor composites and long-term time series are possible. The World Meteorological Organization (WMO) summarizes baseline requirements for satellite-based climate products in (GCOS 2006). It requires for moderate-resolution optical instruments a geolocation accuracy better than 1/3 of the instantaneous field of view (IFOV) in the terrestrial domain.

3. STATE OF THE ART

The following section reviews literature on geolocation accuracy assessment for optical satellite data. Little publications assess the global geolocation accuracy of the 2016 launched OLCI and SLSTR instruments, therefore papers on AVHRR and other sensors are reviewed. In general, two image matching methods exist and are summarized in (Zitová and Flusser 2003). The area-based matching determines the similarity of the image grey level values via cross-correlation. The feature-based technique matches unique and stable features like edges, corners or points. In literature both methods are applied to assess the geolocation accuracy.

3.1 *Geolocation accuracy in support of MODIS land science*

(Wolfe et al. 2002) report on the accuracy of Moderate Resolution Imaging Spectroradiometer (MODIS) satellite data. MODIS was launched in December 1999 on the polar orbiting platform Terra and since February 2000 observes the Earth's surface in 36 spectral bands, with 1 km, 500 m and 250 m nadir pixel size. Terra's on-board exterior orientation measurement system enables geolocation to approximately 150 m at nadir. The MODIS Land science Team requires a geolocation accuracy to be 150 m with an operational goal of 50 m (Nishihama et al. 1997).

A global network of ground control points (GCPs) has been generated in order to assess the biases and trends in the sensor geometry. The estimated biases between MODIS data and GCPs were removed by updating the spacecraft and instrument orientation in the MODIS geolocation software.

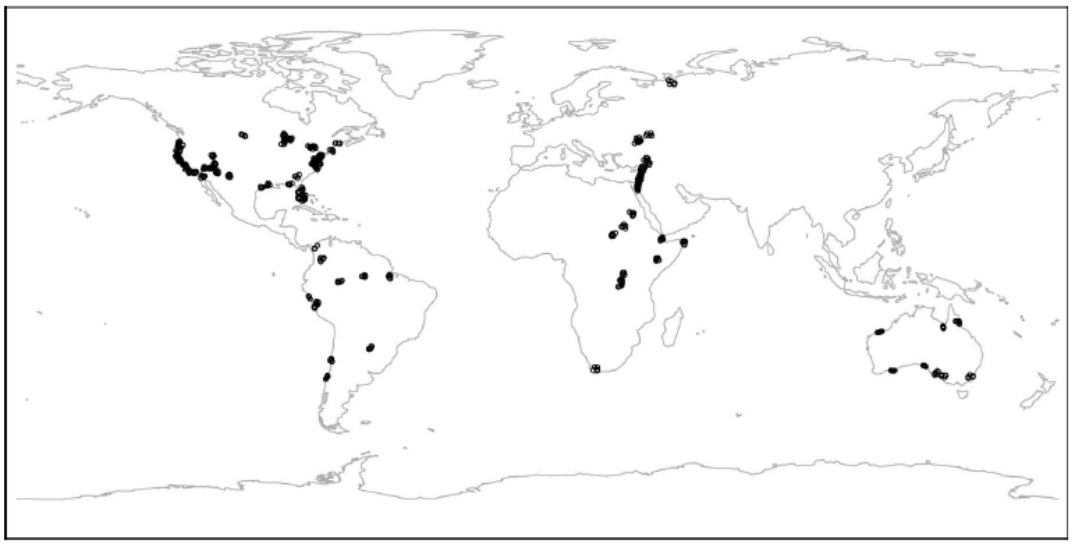

Figure 3-1: Distribution of 420 Ground Control points, derived from 110 Landsat-7 Images. (Wolfe et al. 2002)

The global GCP library is based on 121 Landsat-4 and Landsat-5 precision geolocated terrain corrected TM scenes. For each of the Landsat scenes about 5 GCPs are selected, where the geolocation accuracy of the GCPs is estimated to be in the order of 15 m, corresponding to half of a Landsat Pixel. The image chips were extracted for Landsat band 3 (660 nm) and band 4 (830 nm) and had an extent of about 24 km^2 around the GCP. In order to generate the GCP data base only cloud free Landsat scenes were used. For matching with lower resolution MODIS data, the Landsat image chips were spatially degraded in resolution from about 30 m to 250 m resolution using the MODIS point spread function.

(Wolfe et al. 2002) used MODIS band 1 (620-670 nm) and band 2 (841-876 nm) with 250 m spatial resolution for geolocation assessment with degraded Landsat image chips using normalized image cross correlation. Only those parts of the MODIS swath with a view angle below 45 degrees were used, higher view angles were not considered.

The matching process was performed in several steps

1. Spatially coincident MODIS L1B data, from one of the two 250 m bands, are compared with the corresponding 24 km^2 TM GCP chip. The MODIS line-of-sight is initially computed for the GCP location assuming perfect MODIS geo- location.

2. The TM chip is spatially degraded to 250 m using a MODIS point spread function (Barnes et al. 1998) defined by the sensing geometry of each MODIS 250 m observation intersecting the chip area.
3. Calculation of an area-based correlation is computed between the MODIS 250 m and the TM degraded data applying correlation technique.
4. Step 1-3 is repeated; translating the MODIS data over a regular grid of locations centered on the line-of-sight initially computed assuming perfect MODIS geolocation. The grid point where the maximum correlation occurs defines the final ‘‘true’’ MODIS geolocation. The difference between the true location and the initial location is computed.
5. In order to remove poorly matched GCPs, only those with maximum correlation coefficients greater than 0.6 are considered. In this way inaccurate, out-of-date and out-of-season GCPs, and GCPs contaminated by cloud and aerosols, are less likely to be used.

Based on the geolocation accuracy estimates (Wolfe et al. 2002) applied a deterministic least squares (minimum variance) estimation to compute the sensor orientation parameters that best fit the GCP data. The interior orientation parameters of MODIS sensor could be updated by this way.

3.2 *Suomi NPP VIIRS prelaunch and on-orbit geometric calibration (Wolfe et al. 2013)*

The system developed for MODIS by (Wolfe et al. 2002) was adapted for the Visible Infrared Imaging Radiometer Suite (VIIRS) sensor, which was launched on 28 October 2011 on the Suomi National Polar-orbiting Partnership (SNPP) satellite. The reference data base uses the Landsat 4/5/7 TM GCPs selected for estimating the geolocation accuracy for MODIS but was extended to about 1200 GCPs (Figure 3-2). For matching (Wolfe et al. 2013) used VIIRS band 1 (600 – 680 nm), with a spatial resolution of about 375 m, and the Landsat band at 660 nm. The size of the Landsat image chips is 800 pixels x 800 pixels.

The Landsat Image chips were used to simulate images of VIIRS Band I1 with 375 m nadir resolution with their corresponding projection of idealized line spread functions (LSFs) in triangle or trapezoidal shape in scan direction and evenly distributed in track direction. The simulated images are then correlated with VIIRS images. The shifts of the GCPs at maximum correlation form a series of control point residuals. The residuals are analyzed for corrections of various sensor parameters in the geolocation algorithm. Figure 3-3 shows the geolocation errors in track and scan direction of VIIRS.

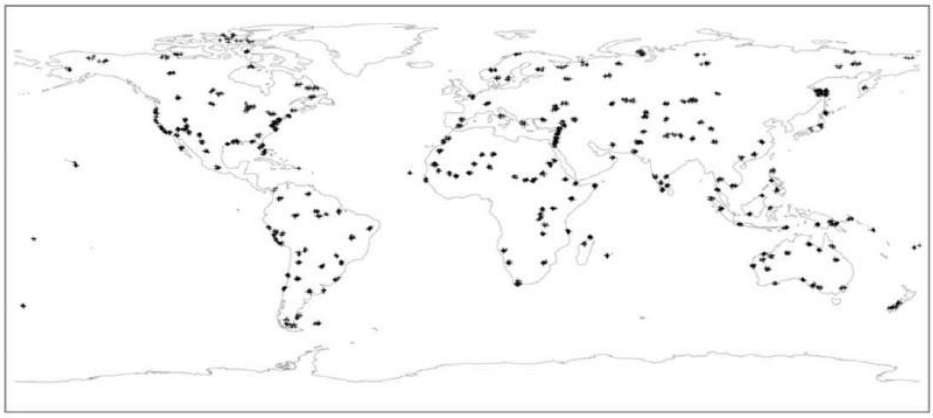

Figure 3-2: Distribution of 1200 globally distributed Ground Control points, derived from Landsat-4, 5 and 7 Images. (Wolfe et al. 2013)

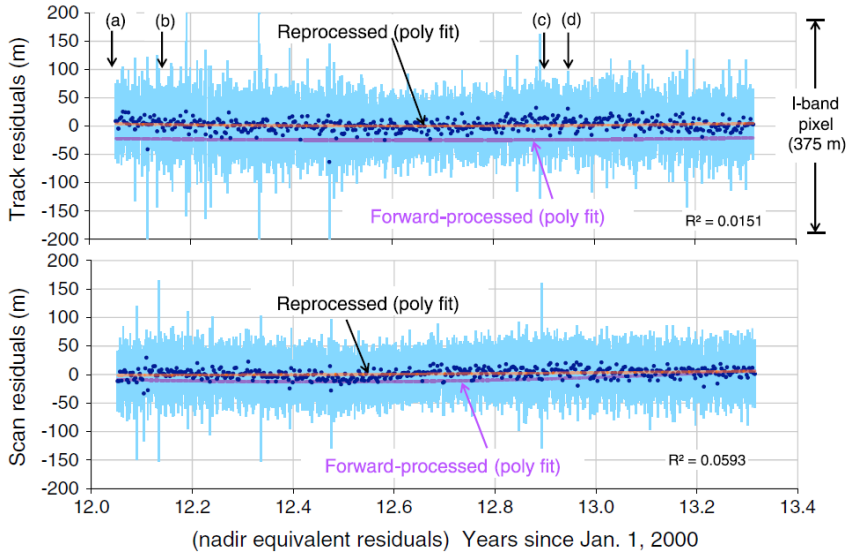

Figure 3-3: Trends of geolocation errors in the track (top graph) and scan (bottom graph) directions. Solid black circles are daily mean. Light vertical bar is the daily standard deviation (nadir equivalent units). (Wolfe et al. 2013)

3.3 *Assessment of the NOAA S-NPP VIIRS Geolocation Reprocessing improvements*

(Wang et al. 2017) review in their paper the improvements in geolocation of the VIIRS I-bands and M-bands. The uncertainty estimation was performed by cross correlation between VIIRS data daytime band I1 (0.639µm) and Landsat red band data with the CPM software. NASA

developed this program originally for MODIS geolocation validation and it has been adopted for VIIRS I-bands. More than 1200 globally distributed image chips with (800 x 800 pixel and 30 m resolution) were processed.

Of interest for the OSMON project is the assessment of the Day-Night-Band (DNB). For VIIRS DNB night-time acquisitions features like lights of oil platforms, powerplants, volcanos, gas flares and bridges were monitored with the CPM Software. The terrain correction introduced on 22 May 2015 improved geolocation at higher altitudes as shown with the example of Lhasa Airport.

3.4 *Subpixel Automatic Navigation of AVHRR (SANA) Scheme*

(Pergola and Tramutoli 2003) developed the SANA (Subpixel Automatic Navigation of AVHRR) system, which is an automatic method for accuracy assessment. SANA is based on an approach suggested by (Rosborough et al. 1994), which corrects satellite attitude parameters on the base of GCPs manually collected over a scene. The SANA system applies this approach fully automatically, progressively correcting the satellite attitude and automatically reducing navigation errors to a pixel level. SANA calculates fully automatically displacements from a 2D correlation analysis between the AVHRR and a reference image.

(Pergola and Tramutoli 2003) applied the SANA system to more than 400 AVHRR scenes, which permits a preliminary evaluation of their performances, dealing with a large collection of test images. The reference image was built using a 30-arc sec resolution Digital Elevation Model to make a georeferenced mask for sea and land locations. The average value of sea and land is computed from the NIR and TIR AVHRR images (cloud free pixels only). The mask and the NIR and TIR images are transformed into the same geographic projection. The comparison between the AVHRR image and the reference data is carried out by calculating a cost function for all cloud free parts of the image. As the cost function is calculated over full scene, one shift is provided for each GCP. The shift was used to correct the navigation parameters.

The accuracy of the navigation algorithm is assessed at 3 small islands with the size of one AVHRR pixel only and known geographic location. The location of the islands in day and night time AVHRR NIR and TIR images was calculated. Figure 3-4 shows the residual navigation error. It shows a clear but weak dependence of the error on the satellite zenith angle.

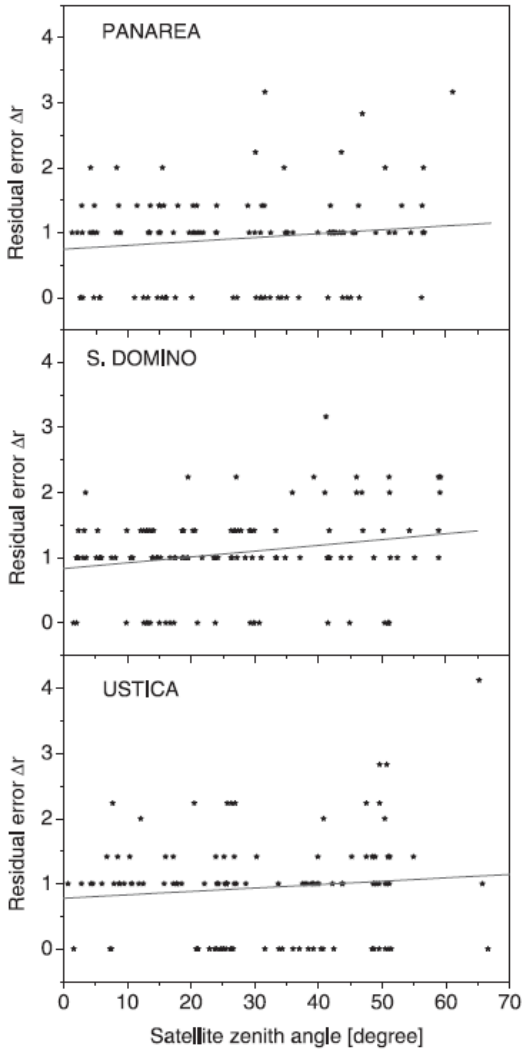

Figure 3-4: Scatterplot of the residual navigation error versus satellite zenith angles for 3 islands. (Pergola and Tramutoli 2003)

3.5 *AVHRR – contour-matching*

(Eugenio and Marqués 2003) published an automatic satellite image georeferencing method for AVHRR data. They combined an orbital prediction model, which provides initial earth locations combined with an automatic contour matching method. It allows correcting low frequency errors mainly due to timing and orbital errors as well as the high frequency error due to variations in spacecraft attitude. The contour matching process has three major steps, 1) estimation of the gradient energy map and detection of cloudless areas; 2) initialization of contour positions, and 3) the estimation of the transformation parameters using a contour optimization approach. The procedure

steps are shown in Figure 3-5. Three automatic optimization algorithms were tested, and their performance was assessed using AVHRR data.

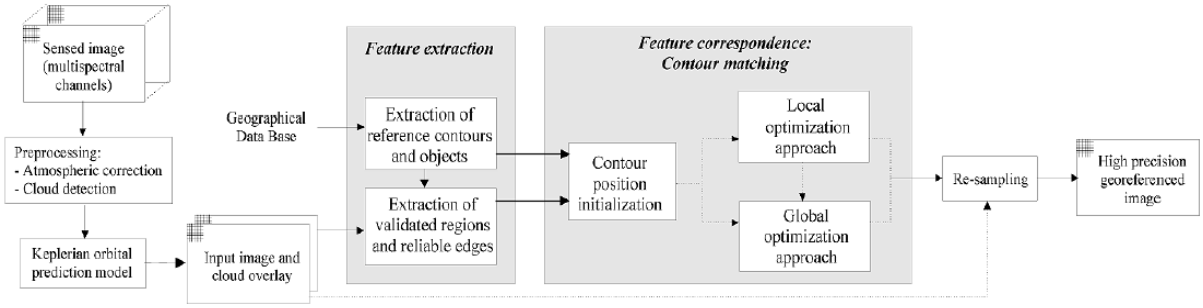

Figure 3-5: Schematic procedure of the proposed automatic contour matching system. (Eugenio and Marqués 2003)

The reference image defining the reference contours is created from a geographical database. Eugenio and Marques (2003) obtained the reference image from the Central Intelligence Agency World Data Base II. In the input AVHRR image, reliable edges associated to sea-land transitions are extracted.

The applied contour matching approaches are iterative energy minimization processes. For each reference object, the reference contour position leading to the minimum energy is searched.

3.6 *Achieving Subpixel Accuracy in Canadian AVHRR Processing System (CAPS)*

(Khlopenkov et al. 2010) developed a GCP correction for AVHRR data in order to achieve an accuracy of 1/3 FOV.

Clear-sky MODIS Level 1B products at 250 m spatial resolution were used as reference images for the geolocation correction of a historical time series of AVHRR data with 1 km spatial resolution. To avoid extrapolation errors by resampling the swath image into a geographical projection, the orthorectification was performed in the swath projection. For orthorectification, a DEM at 250 m spatial resolution was employed.

In the implemented image matching procedure, the swath image was matched to a specially prepared reference image. For each month an own reference image was used in order to account for the seasonal variability of surface properties. The NIR channel was used because of a high spectral contrast

between different surface types, such as water and land. The reference images were aggregated to the resolution of the swath images of 1 km in order to achieve a high accuracy of image matching.

The procedure of image matching was performed at noticeable landmarks with high spatial contrast, such as rivers, hills and coastlines, which are called GCPs. An automated GCP selection routine, which locates the areas of highest spatial variability, was implemented. Additionally, a uniform spatial coverage of the selected map region by the GCPs was considered.

The image matching procedure was performed in the swath domain (i.e., pixel-line coordinate system). Therefore, the reference image was reprojected from the map projection to swath coordinates. To receive a better resemblance between the reprojected reference image and the original swath image, the effect of the point-spread function (PSF) of the AVHRR instrument was included. However, the two images can still differ significantly due to clouds, shadows, annual variations of reflectance and snow cover and other external effects. In order to minimize the influence of these effects, the images were processed with the Laplacian operator, which enhances small-scale features like rivers and coastlines, whereas larger and smoother objects like clouds are suppressed.

The image matching routine then calculated the covariance between the reference image and the original swath image for different displacements within the expected range. The resulting covariance matrix was scaled between 0 and 255. The optimal displacement between the images was determined by the location of the maximum of the covariance matrix. Figure 3-6 shows a comparison of the covariance matrix for a cloudy GCP with and without application of the Laplacian operator.

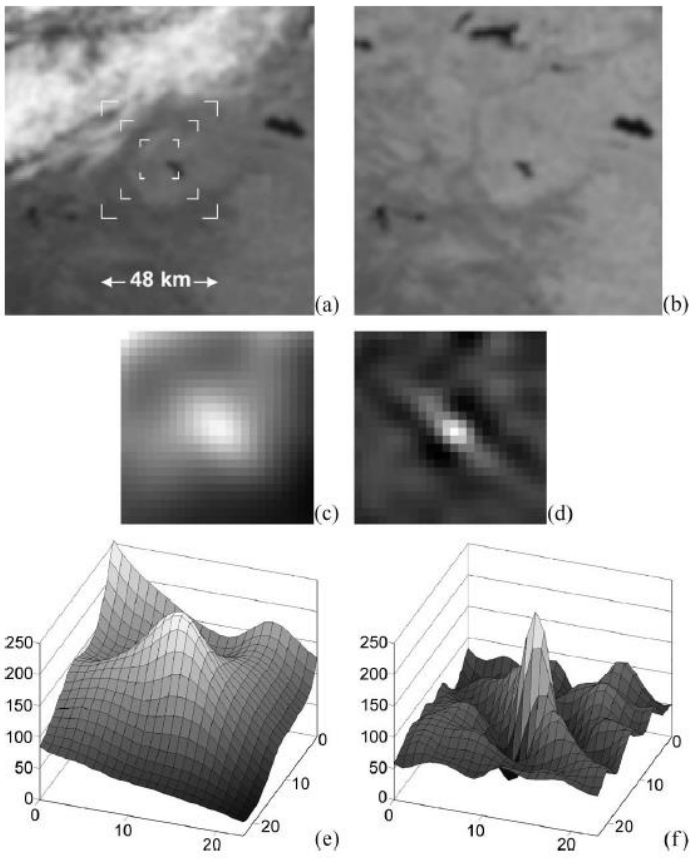

Figure 3-6: Example of AVHRR NOAA-17 image contaminated by clouds. (a) Image observed by AVHRR. (b) Reprojected reference MODIS image. [(c) and (e)] Covariance matrix for the original images. [(d) and (f)] Covariance matrix for the Laplacian images. (Khlopenkov et al. 2010)

For the achievement of subpixel accuracy, a third-order polynomial surface was fitted through the points of the covariance matrix and solved analytically to find the subpixel location of the maximum.

In order to avoid the influence of false apexes in the covariance matrix, which can be stronger than the real apex in some complex scenes, a special filter was introduced. Therefore, the mathematical mean of the covariance matrix as well as the level of covariance along a circumference around the main apex was used.

The derived statistics of GCP displacements were used to estimate the accuracy of the image matching procedure. Figure 3-7 shows the results over North America for a winter period in February 1995.

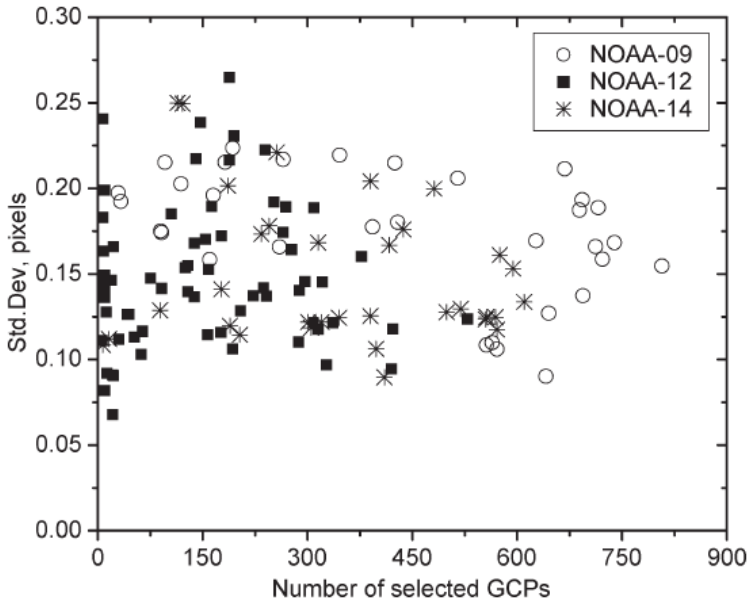

Figure 3-7: Example of CAPS testing over the period of February 21-28, 1995, for AVHRR on NOAA-9, 12, and 14. (Khlopenkov et al. 2010)

3.7 *Automated Improvement of Geolocation Accuracy by chip matching approach*

In the German Aerospace Center (DLR) TIMELINE project precise geolocated AVHRR data are used to compose timeseries since the early 1980s utilizing all three AVHRR sensor generations. To reduce the geolocation uncertainty of up to 10 km per pixel (Dietz, et al., 2017) estimated the shift of the AVHRR data in two steps after cloud mask delineation. A cloud mask and cloud parameters are extracted from AVHRR data with APOLLO_NG algorithm. If the cloud cover is less than 8% in the image chip it is approved for the matching. The matching is performed in orbit projection.

First the shift with respect to a predefined reference water mask was estimated. The water mask was derived from data provided by naturalearth.com (based on World data bank 2 inventory and updated with a pan-European River and Catchment Database provided by the Joint Research Centre, JRC). The mask was resampled to 0.01° resolution. Around 400 unmistakable distinguishable image chips of waterbodies with pronounced features were selected and correlated.

In the second step the match was performed on the median of the Normalized Vegetation index (NDVI). The NDVI mask was derived from the MODIS operational Vegetation Indices Monthly L3 Global 1 km dataset MOD13.

Only if both image correlations result in a consistent shift, in any direction a shift vector was estimated.

With the shift vectors a third order polynomial was set up and applied to lat/lon grid of the satellite data, while the image remained unchanged. Validation showed aa reduced average uncertainty from 1.6 km to 0.92 km. The most critical point is cloud coverage which varies significantly across Europe with values of average cloud cover fractions between 40 % in Italy and 70 % in Sweden. The presented algorithm can generally be also applied outside Europe.

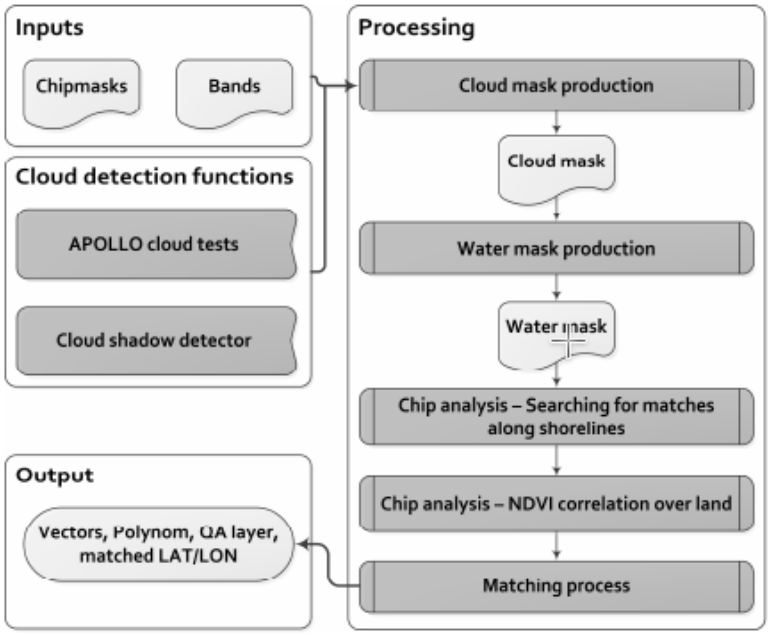

Figure 3-8 Steps of chip-matching algorithm (Dietz et al. 2017)

3.8 *Geometric Quality Analysis of AVHRR Orthoimages*

The objective of the research by (Aksakal et al. 2015) was to analyze the geometric accuracy of the satellite sensors SEVIRI (Spinning Enhanced Visible and Infrared Imager), MODIS (Moderate Resolution Imaging Spectroradiometer) and AVHRR (Advanced Very High Resolution Radiometer) for systematic observation of Essential Climate Variables (ECVs). Relative, absolute and band-to-band registration (BBR) accuracies of the AVHRR orthoimages were estimated with the Kanade-Lukas-Tomasi (KLT) point matching method. It has been demonstrated in (Aksakal 2013) for Imagery of the SEVIRI instrument on board of the geostationary satellites Meteosat-8 and Meteosat-9. This method is implemented in Python's OpenCV package.

The following pre-processing steps enhanced the image contrast and reduced large radiometric differences. After loading the image its histogram was linearly stretched and converted from 16-bit to 8-bit. Then the cloud mask was extracted. The KLT tracking was applied to a large number of patches with a size of 15x15 pixels of AVHRR Band-2 images of the same day. For the assessment of absolute accuracy lakes with a cloud cover less than 60% in Band-2 were used. The lakes were matched with 20 lakes digitalized from Landsat -5 images. The shifts are calculated in northing and easting direction, showing maximal shifts of 4 pixel in MetOp-A, 1.6 pixel in NOAA-17 and 1 pixel in NOAA-18 images. An increase in standard deviation in off-nadir images was observed with values up to 0.7 pixel. The mean shifts are summarized in the following table:

Table 3-1 Summarized absolute AVHRR (Band-2) shifts in pixel

	Mean shift		*Shift standard deviation*	
	x (east)	y (north)	x (east)	y (north)
NOAA-17	0.2	-0.2	0.3	0.2
NOAA-18	0.1	-0.3	0.2	0.2
MetOp-A	-0.1	-0.4	0.4	1.1

3.9 *Geolocation assessment of MERIS GLOBCOVER ortho-rectified products*

The GLOBCOVER project, which delivers a global land cover map at 300 m spatial resolution, uses fine resolution (300 m) mode data (FRS) from the MERIS sensor on-board the ENVISAT satellite. The requirement of the GLOBCOVER project is an absolute and relative geometric accuracy better than 150 m. Therefore, an assessment of the geolocation accuracy of MERIS projected products was performed by (Bicheron et al. 2008).

For the relative validation, the ortho-rectified MERIS products were compared to MERIS products acquired over the same area at different time in order to verify the co-registration accuracy.

For the verification of absolute geo-location accuracy, LANDSAT ETM+ data with a spatial resolution of 30 m and a RMSE accuracy inferior to 50 m were used as reference products. To achieve a similar resolution with the MERIS data, LANDSAT images were re-sampled to 300 m. LANDSAT band B4 (760-900nm) was compared to MERIS band 13 (865 nm).

For the comparison of the reference image and the ortho-rectified MERIS product, the correlation tool MEDICIS, which was developed by the French company CS (Communications and Systems), was used. This tool computes a similarity measurement between the master image (reference image) and the

slave image, which is successively translated regarding the master image. By evaluating the translation that maximizes the similarity criterion between the two images, the shifts in line and column are determined.

The sites which were used for the assessment of the geo-location errors were selected considering different latitudes, acquisition time and topography, low cloud coverage, high revisiting rate and different longitudes. According to these criteria, 5 sites were selected.

Both relative and absolute validation showed a RMSE smaller than 150 m. The RMSE in longitude and latitude resulting from the absolute geo-location accuracy is shown in Figure 3-9.

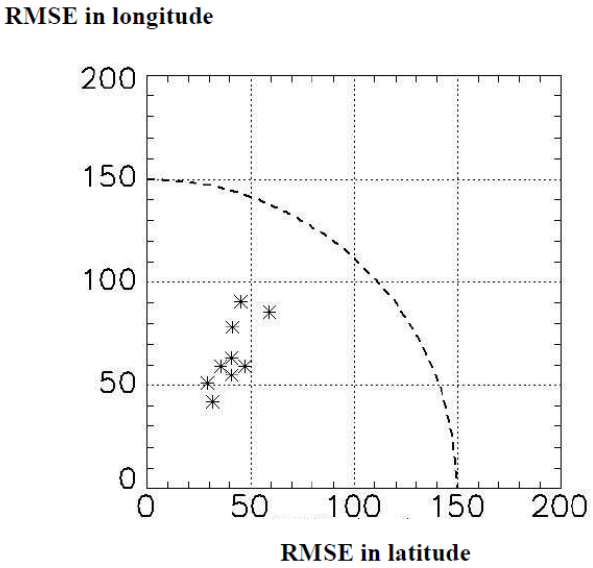

Figure 3-9: RMSE in longitude as a function of RMSE in latitude (unit = meter). A star symbol represents one couple of images. The semi-circle represents the threshold of values required by the GLOBCOVER project. (Bicheron et al. 2008)

3.10 *Geometric accuracy of the orthorectification process from GeoEye-1 and WorldView_2 panchromatic images*

(Aguilar et al. 2013) studied the geometric accuracy of the panchromatic (PAN) images of the very high resolution (VHR) satellites GeoEye-1 and WorldView-2.

GeoEye-1, which was launched in September 2008, has a Ground Sample Distance (GSD) of 0.41 m at nadir in PAN imagery. WorldView-2 was launched in October 2009 and collects PAN images with a pixel size of 0.46 m at nadir. However, the PAN image products from both satellites are down-sampled to 0.5 m due to a U.S. governmental requirement.

The study area for the accuracy assessment is located on the East coast of Southern Spain. A set of 44 ground control points (GCPs) and 75 Independent Check Points (ICPs), located on well-defined features and homogeneously distributed over the study area was prepared (see Figure 3-10), with an accuracy better than a decimeter.

Figure 3-10: Distribution of 75 ICPs (black crosses) and 44 GCPs (white circles) overlaid on a GeoEye-1 panchromatic orthorectified image. (Aguilar et al. 2013)

The GCPs were used for the computation of the different geometric sensor models for the relation of the three-dimensional object space positions to their corresponding two-dimensional image space positions.

On the other hand, the ICPs were only applied in the assessment of the geopositioning capabilities of orthorectified GeoEye-1 and WV-2 PAN images.

The accuracy assessment was carried out depending on the following factors:

1. the type of input VHR satellite PAN image
2. the sensor model

3. the number of well-distributed GCPs used in the triangulation process
4. the off-nadir viewing angle ranging from 5° to 23.1°
5. the vertical accuracy of the DEM employed in the orthorectification process

In order to study the influence of these factors, an analysis of variance (ANOVA) test was carried out, with the planimetric root mean square error ($RMSE_{2D}$) as observed variable.

Concerning the sensor model, the best horizontal geopositioning accuracies were attained by using third order 3D rational functions with vendor's rational polynomial coefficients data refined by a zero-order polynomial adjustment (RPC0). Additionally, the ANOVA statistical tests revealed a high dependence of the geolocation accuracy on the off-nadir angle, which is related to the GSD. Figure 3-11 shows the relationship between the GSD and the accuracy attained at the sensor orientation phase by using the sensor model RPC0 for GeoEye-1 Geo and WV-2 ORS2A images. Furthermore, the accuracy of the DEM showed a significant influence on the geopositioning accuracy.

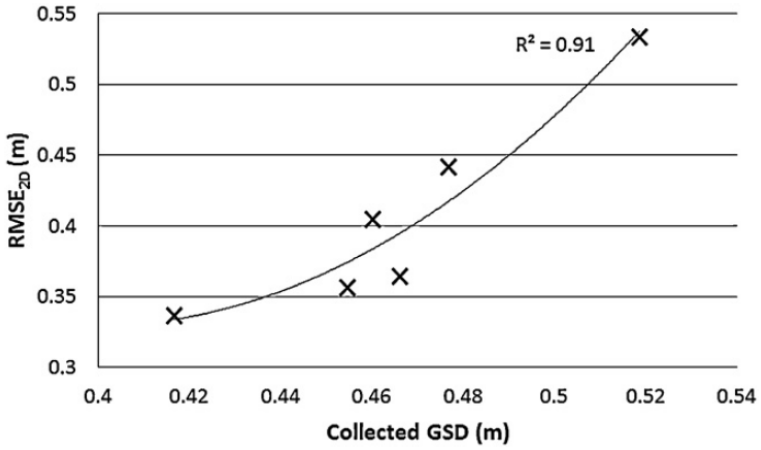

Figure 3-11: Relationship between the collected GSD and the $RMSE_{2D}$ attained at the sensor orientation phase by using RPC0 for GeoEye-1 Geo and WV-2 ORS2A images. (Aguilar et al. 2013)

3.11 *Absolute and relative geolocation accuracies of QB01 and WV01*

QuickBird-2 (QB02), launched in October 2001, and WorldView-1 (WV01), launched in September 2007, are high resolution imaging satellites operated by DigitalGlobe. QB02 has four multispectral bands and one panchromatic band. The PAN band, which has a 0.61 m GSD at nadir, is used for the assessment of the absolute geolocation accuracy. WV01 is a PAN only satellite with a 0.590 m GSD at

nadir. The geolocation accuracies of both satellites are assessed twice a month. The geolocation statistics from a two year period from 2006 to 2008 are presented by (Smiley 2009).

A set of 30 ground control point (GCP) collections (called “geocal sites”), with 7 – 104 GCPs each, is used to measure the geolocation accuracy of QB02 and WV01 imagery. All GCPs are surveyed to sub-meter accuracy, where most of them have an accuracy of 25 cm. The GCPs have thorough latitude coverage of about 2 GCPs every 10 degrees of latitude.

For the calculation of the geolocation error of a GCP, the image coordinates (i.e., the line (row) and pixel (column) location) of that point must be determined and recorded. This can be done manually by comparing the imagery to a sketchbook for the GCPs, or automatically with image recognition routines comparing the imagery to small reference images collected in advance. The determined image coordinates for each GCP are projected to the ground, using the rigorous camera model for the appropriate satellite. From the difference between the projected GCP location and the surveyed coordinates of the GCP, the absolute geolocation error of a GCP (“full geolocation error”) can be retrieved. In addition, the full geolocation error is scaled back to nadir in order to retrieve the “nadir projected error”, which is used to estimate the amount of geolocation error inherent in the satellite’s hardware.

In order to calculate the absolute accuracy of an entire geocal strip, the average geolocation error of that strip is used. The magnitude of the average geolocation error is the measure of absolute geolocation accuracy. Furthermore, the relative geolocation accuracy of an image strip is examined as the change of the absolute geolocation errors within an image by systematically calculating the vector differences between all pairs of absolute errors in the image. The worst relative error is used to represent the relative geolocation accuracy of a strip. An example of the nadir projected absolute error, average error and worst relative error is shown in 3-12.

For the determination of the geolocation accuracy of a satellite, the geolocation accuracies of geocal strips are statistically analyzed over time.

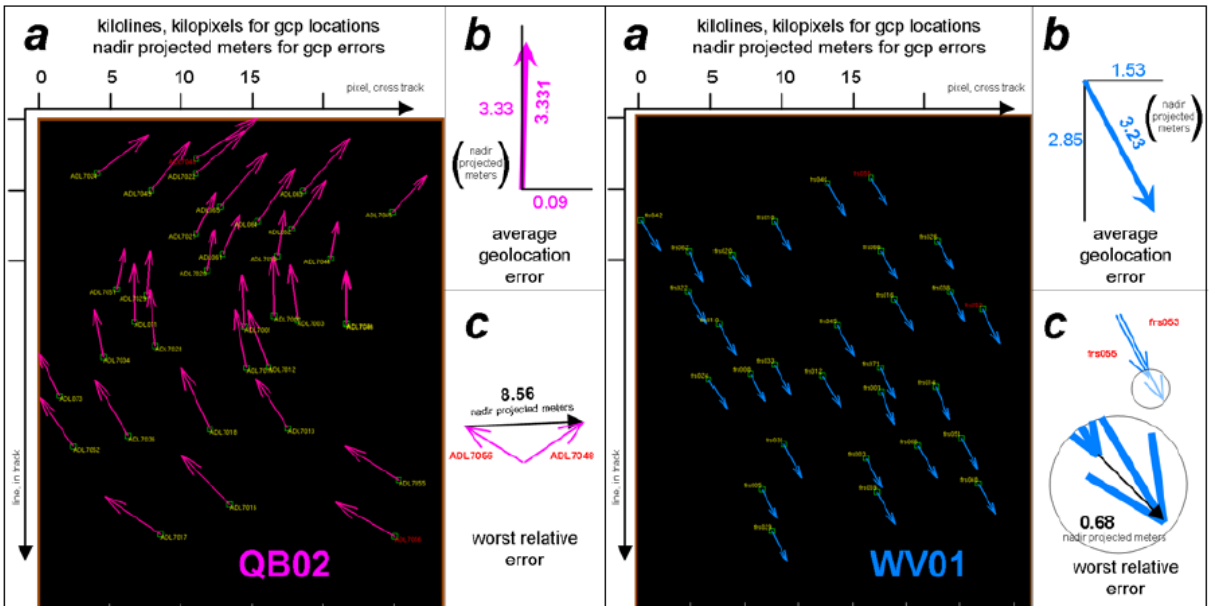

3-12: (a) Sample quiver plot for QB02 (left) and WV01 (right) using nadir projected errors. (b) Average geolocation error. (c) worst relative error.

3.12 *ESA QA4EO GEOACCA - Feasibility Study for Geolocation Assessment of Medium Resolution Optical Sensors*

Within the GEOACCA project ENVEO developed an automatic system for estimating the geolocation accuracy of medium resolution optical sensors ((Nagler et al., 2016; https://geoacca.enveo.at/). The system consists of the modules,

- a module for estimating the geolocation accuracy at GCPs using cross-correlation
- a relational data base system storing GCPs, the estimated geolocation accuracy and quality at GCPs for overflights (including quicklooks)
- analysis and visualization tool of geolocation accessible via internet.

The GCP data base consist of 394 manually selected globally distributed targets, primarily lakes and islands (Figure 3.13). For each of the GCPs image chips were extracted from Landsat Images (Figure 3.14). For calculating the shifts of the medium resolution optical data set and the Landsat image chip at the GCP, the medium resolution optical data were resampled to the pixel spacing of Landsat using bilinear interpolation. The processing system was implemented in python 2.7, uses a POSTGRES data base for managing GCPs and estimated image shifts, and uses DJANGO for the web-based visualisation and analysis tool.

The system was applied to the full mission ATSR-2, AATSR and MERIS data set, as well as selected years of PROBA-V Vegetation. Example of the AATSR geolocation analysis is given in Figure 3.15.

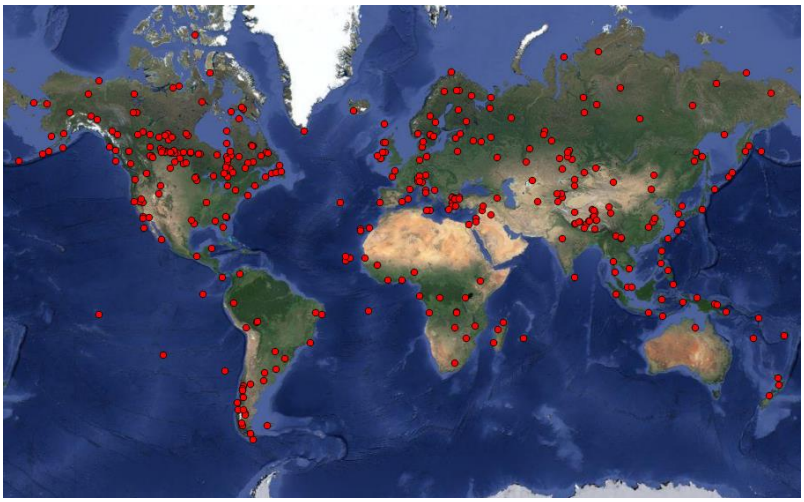

Figure 3.13: Location of GCPs of database version 1.1.0.

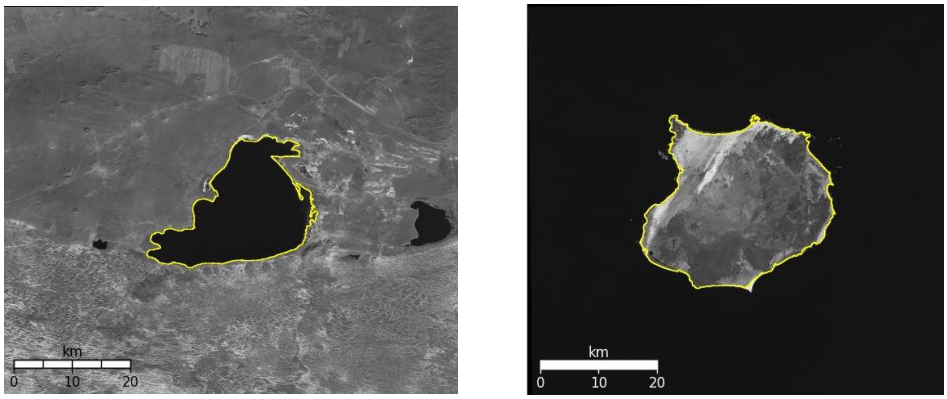

Figure 3.14: Examples of Ground Control Points, displayed by the SWBD water outlines laid over the Landsat band 4 (NIR) raster files: The lake Dali Nuoer in China (left), and the island Ilha da Boa Vista in Cap Verde, Africa (right).

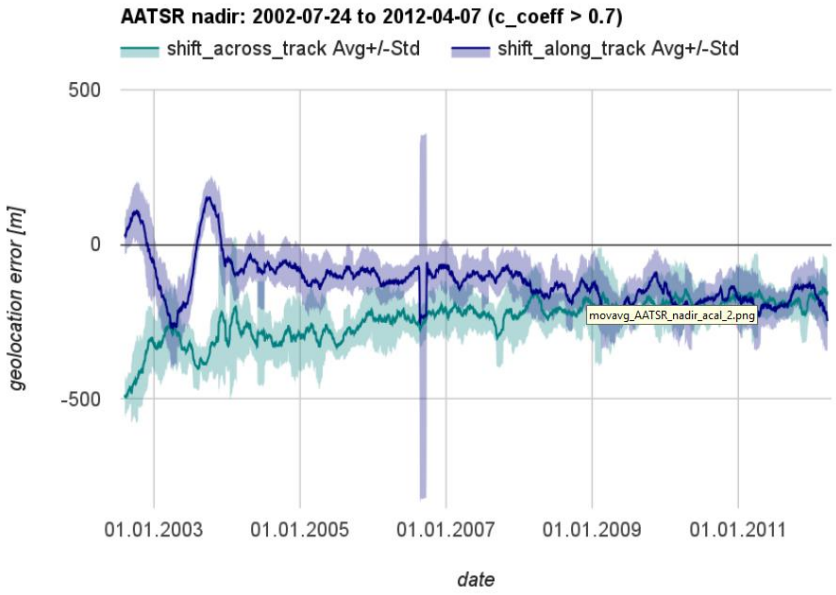

Figure 3.15: Example of report on geolocation accuracy of AATSR, nadir view, generated by ENVEO within GEOACCA project. It shows the 35-day moving average +/- standard deviation of across-track and along-track geolocation error for AATSR nadir data based on shifts with matches of correlation coefficient above 0.7.

4. CONCLUSION AND A WAY FORWARD

4.1 *Conclusions*

In literature geolocation assessment utilizes area-based and feature based matching methods. For OSMON we estimate the uncertainty in northing and easting direction (UTM) and not in swath geometry. By computing the 2d shift between the satellite image and a reference image the absolute accuracy is estimated. Lakes and islands show good contrast compared to the surroundings in NIR-Band and are thus selected as GCP. Water masks form SRTM, TanDEM-X and Natural Earth (www.naturalearthdata.com) help to select proper points. A global catalogue of roughly 500 equally distributed GCPs will be set up. It is based on the existing GEOACCA-database. GCPs are selected from terrain corrected Landsat 8 L1T as well as Sentinel-2 products depending on cloud cover. In the deserts we suggest selecting distinct changes in geology like in the Aïr Mountains in northern Niger. These areas

4.2 *Software Tools*

(Aksakal 2013; Aksakal et al. 2015; Scheffler et al. 2017; Skakun et al. 2017) base their investigations on Python and its OpenCV image processing package to perform the lake matching and the statistical analysis. (Skakun et al. 2017) exploit an efficient subpixel image registration algorithm introduced by (Guizar-Sicairos et al. 2008). It is implemented in Pythons scikit-image package and uses a cross-correlation approach in the frequency domain. To distinguish cloud covered GCPs from clear sky scenes (Dietz et al. 2017) use the APOLLO (AVHRR Processing Over cLouds, Land and Ocean) algorithm. (Zhu and Woodcock 2012) apply the opens-source Python Fmask module to mask clouds.

5. REFERENCES

Aguilar, M. a., M. D. M. Saldaña, and F. J. Aguilar, 2013: Assessing geometric accuracy of the orthorectification process from GeoEye-1 and WorldView-2 panchromatic images. *International Journal of Applied Earth Observation and Geoinformation*, **21**, 427–435, doi:10.1016/j.jag.2012.06.004.

Aksakal, S., 2013: Geometric Accuracy Investigations of SEVIRI High Resolution Visible (HRV) Level 1.5 Imagery. *Remote Sensing*, **5**, 2475–2491, doi:10.3390/rs5052475.

Aksakal, S., C. Neuhaus, E. Baltsavias, and K. Schindler, 2015: Geometric Quality Analysis of AVHRR Orthoimages. *Remote Sensing*, **7**, 3293–3319, doi:10.3390/rs70303293.

Barnes, W. L., T. S. Pagano, and V. V Salomonson, 1998: Prelaunch characteristics of the Moderate Resolution Imaging Spectroradiometer (MODIS) on EOS-AM1. *Geoscience and Remote Sensing, IEEE Transactions on*, **36**, 1088–1100, doi:10.1109/36.700993.

Bicheron, P., and Coauthors, 2008: Geolocation assessment of 300 m resolution meris globcover ortho- rectified products. *Proc. of the "2nd MERIS / (A)ATSR User Workshop", Frascati, Italy,*.

Dietz, A., C. Frey, T. Ruppert, M. Bachmann, C. Kuenzer, and S. Dech, 2017: Automated Improvement of Geolocation Accuracy in AVHRR Data Using a Two-Step Chip Matching Approach—A Part of the TIMELINE Preprocessor. *Remote Sensing*, **9**, 303, doi:10.3390/rs9040303.

Eugenio, F., and F. Marqués, 2003: Automatic Satellite Image Georeferencing Using a Contour-Matching Approach. *IEEE Transactions on Geoscience and Remote Sensing*, **41**, 2869–2880.

GCOS, 2006: Systematic observation requirements for satellite-based products for climate-Supplemental details to the satellite-based component of the "Implementation Plan for the Global Observing System for Climate in Support of the UNFCCC." *Technical Report GCOS-107, WMO/TD No 1338*,.

Guizar-Sicairos, M., S. T. Thurman, and J. R. Fienup, 2008: Efficient subpixel image registration algorithms. *Optics Letters*, **33**, 156, doi:10.1364/OL.33.000156.

Khlopenkov, K. V, A. P. Trishchenko, and Y. Luo, 2010: Achieving Subpixel Georeferencing Accuracy in the Canadian AVHRR Processing System. *IEEE Transactions on Geoscience and Remote Sensing*, **48**, 2150–2161.

Nagler, T., U. Blumthaler, and P. Malcher, 2016: Feasibility study for geolocation assessment of optical sensors. Final Report and Evolution of tool. ESA Study Contract 4000108867/13/I-BG.

Nishihama, M., R. Wolfe, D. Solomon, F. Patt, J. Blanchette, A. Fleig, and E. Masuoka, 1997: MODIS Level 1A Earth Location: Algorithm Theoretical Basis Document Version 3.0, SDST-092, Lab. Terrestrial Phys. Greenbelt, MD: NASA Goddard Space Flight Center.

Pergola, N., and V. Tramutoli, 2003: Two years of operational use of Subpixel Automatic Navigation of AVHRR scheme: accuracy assessment and validation. *Remote Sensing of Environment*, **85**, 190–203, doi:10.1016/S0034-4257(02)00205-5.

Rosborough, G. W., D. G. Baldwin, and W. J. Emery, 1994: Precise AVHRR image navigation. *Geoscience and Remote Sensing, IEEE Transactions on*, **32**, 644–657, doi:10.1109/36.297982.

Scheffler, D., A. Hollstein, H. Diedrich, K. Segl, and P. Hostert, 2017: AROSICS: An Automated and Robust Open-Source Image Co-Registration Software for Multi-Sensor Satellite Data. *Remote Sensing*, **9**, 676, doi:10.3390/rs9070676.

Skakun, S., J.-C. Roger, E. F. Vermote, J. G. Masek, and C. O. Justice, 2017: Automatic sub-pixel co-registration of Landsat-8 Operational Land Imager and Sentinel-2A Multi-Spectral Instrument images using phase correlation and machine learning based mapping. *International Journal of Digital Earth*, **10**, 1253–1269, doi:10.1080/17538947.2017.1304586.

Smiley, B., 2009: The absolute and relative geolocation accuracies of QB02 and WV01. *ASPRS 2009 Annual Conference Baltimore, Maryland ŠMarch*, 9–13.

Wang, W., C. Cao, Y. Bai, S. Blonski, and M. Schull, 2017: Assessment of the NOAA S-NPP VIIRS Geolocation Reprocessing Improvements. *Remote Sensing*, **9**, 974, doi:10.3390/rs9100974.

Wolfe, R. E., M. Nishihama, A. J. Fleig, J. a. Kuyper, D. P. Roy, J. C. Storey, and F. S. Patt, 2002: Achieving sub-pixel geolocation accuracy in support of MODIS land science. *Remote Sensing of Environment*, **83**, 31–49, doi:10.1016/S0034-4257(02)00085-8.

Wolfe, R. E., G. Lin, M. Nishihama, K. P. Tewari, J. C. Tilton, and A. R. Isaacman, 2013: Suomi NPP VIIRS prelaunch and on-orbit geometric calibration and characterization. *Journal of Geophysical Research: Atmospheres*, **118**, 11,508-11,521, doi:10.1002/jgrd.50873.

Zhu, Z., and C. E. Woodcock, 2012: Object-based cloud and cloud shadow detection in Landsat imagery. *Remote Sensing of Environment*, **118**, 83–94, doi:10.1016/j.rse.2011.10.028.

Zitová, B., and J. Flusser, 2003: Image registration methods: a survey. *Image and Vision Computing*, **21**, 977–1000, doi:10.1016/S0262-8856(03)00137-9.